RESEARCH ARTICLE OPEN ACCESS

Comparative Electrochemical and Mechanical Investigation of Alkali Ion Insertion into Berlin Green

Filiz-Pinar Seren | Tolga Akçay | Iurii Panasenko | Fabian Jeschull | Dominik Kramer | Reiner Mönig

Institute for Applied Materials, Karlsruhe Institute of Technology, Eggenstein-Leopoldshafen, Germany

Correspondence: Filiz-Pinar Seren (filiz-pinar.seren@kit.edu)

Received: 16 March 2026 | **Revised:** 22 May 2026 | **Accepted:** 28 May 2026

Keywords: ion exchange | operando characterization | Prussian Blue analog (PBA) | reaction mechanism | substrate curvature measurement

ABSTRACT

Stable electrode materials with reversible ion insertion/extraction are central to developing sodium- and potassium-ion batteries as lithium-ion alternatives. Here, we investigated the impact of different monovalent insertion ions on the performance and reliability of the same electrode. We chose Berlin Green (BG, $Fe^{III}[Fe^{III}(CN)_6]$), a Prussian Blue analog (PBA), due to its rigid structure, ability to accommodate different ion sizes, and two different redox-active Fe atoms. We conducted electrochemical tests, intermittent scanning electron microscopy (SEM), and *operando* substrate curvature experiments on BG as we changed the counter electrode and electrolyte. With this novel experimental strategy, we report for the first time sequential insertion/extraction of all three ions in/from the same single BG electrode, eliminating electrode variations and ensuring direct comparability of ion insertion, degradation, and stress. While Li^+ and Na^+ follow comparable pathways, K^+ leads to distinct electrochemical and mechanical responses, underscoring ion-specific interactions within the host framework. We demonstrate that BG enables highly reversible insertion/extraction with a high tolerance to ionic size variation and great surface stability, despite volume changes and phase transitions. These results position BG as a model system for understanding alkali ion insertion and as a versatile and sustainable electrode material for future energy storage systems.

1 | Introduction

Growing concerns about the energy crisis and rising global energy consumption are driving demand for environmentally friendly and sustainable energy generation and storage technologies [1]. Monovalent metal-ion batteries, particularly lithium-ion batteries (LIBs), play a key role as energy storage systems [2]. Since their breakthrough in 1991 with the development of carbon-based negative electrodes [3], LIBs have become the most successful and efficient electrochemical energy storage systems, powering portable electronic devices and electric vehicles thanks to their high energy densities and long cycle life [4]. However, increasing demand for LIBs has raised concerns regarding the availability and rising cost of Li [5]. In contrast to the low abundance of lithium (Li, 0.0017 wt% [6]) in the Earth's crust, sodium (Na, 2.3 wt% [6]) and potassium (K, 1.5 wt% [6]) offer higher availability and therefore potential low cost, driving growing interest in Na-ion (SIBs) and K-ion batteries (KIBs), especially for stationary energy storage [2, 7]. Being alkali metals, Li, Na, and K share similar physical and chemical properties, which allows for the transfer of the established technical understanding of LIBs to accelerate the development of SIBs and KIBs [8]. SIBs are very promising low-cost candidates to complement LIBs as large-scale energy storage systems. However, the standard electrochemical potential of Na^+/Na is 0.33 V higher than that of Li^+/Li and may result in lower operating voltages and lower energy densities of Na-based systems compared to Li [9]. The larger ionic radius of Na compared to Li may lead to increased volume changes and unfavorable phase transitions during cycling, resulting in rapid capacity decline. Therefore, alternative electrode materials compatible with Na^+ ions are required. KIBs have attracted interest as alternatives to LIBs due to a K^+/K standard redox potential of

only 0.1 V higher than that of Li^+/Li [8]. In organic electrolytes, the potential of K^+/K can be even lower (by −0.1 V) than that of Li^+/Li [10]. These low potentials allow for high operating voltages and competitive energy densities [11]. Solvated K^+ ions have a smaller Stokes radius than Li^+ and Na^+ ions, resulting in higher ionic conductivity and improved kinetics of K electrolytes [12]. However, compared to Li and Na, K has the largest ionic radius, which can introduce structural instability during cycling and faster capacity fade. As in SIBs, identifying electrode materials that can reversibly accommodate the insertion ions remains an outstanding challenge [13, 14].

Among various cathode candidates, Prussian Blue analogs (PBAs) have been extensively investigated for their low-cost, tunable redox potentials, open framework, scalable synthesis, and absence of critical metals [15]. PBAs are metal–organic frameworks that exhibit perovskite-type and often face-centered cubic (fcc) structures with the space group $Fm\bar{3}m$ [16]. PBAs can be described using the general chemical formula $A_xT[M(CN)_6]_y$ ($0 \le x \le 2$; $0 < y < 1$), where A represents the alkali ion, and T and M denote transition metals [14]. These transition metals form TN_6 and MC_6 octahedra bridged by cyanide groups ($^-C{\equiv}N$), creating a three-dimensional open framework that facilitates ion transport of various monovalent and even multivalent ions. PBAs prepared by conventional precipitation synthesis contain large amounts of $M(CN)_6$ vacancies in the framework, occupied by coordinated water. Thus, PBAs can be described by the more accurate chemical formula $A_xT[M(CN)_6]_{1-y} \cdot \square_y \cdot nH_2O$ ($0 \le x \le 2; 0 < y < 1$), where □ represents vacancies. Coordinated water is chemically bonded with the unsaturated transition metal ion and harder to remove, unlike adsorbed water on the surface and zeolitic water in interstitial sites, which can be removed by drying [17, 18]. The water destabilizes the lattice, blocks ion transport channels, and limits electrochemical performance [19, 20]. One of the earliest and most researched hexacyanoferrates is Prussian Blue (PB, $AFe^{III}Fe^{II}(CN)_6$ for soluble PB), with a cubic structure and iron (Fe) at both sites as redox-active centers [18, 21]. PB can reversibly accommodate metal ions through two distinct redox reactions, leading to the formation of two additional phases: Berlin Green (BG, $Fe^{III}Fe^{III}(CN)_6$) and Prussian White (PW, $A_2Fe^{II}Fe^{II}(CN)_6$). During ion insertion, BG undergoes sequential redox reactions: first, a phase transformation from BG to PB and subsequently, from PB to PW. In PW, all Fe ions are reduced to the +II state, while in BG, all of them are oxidized to the +III state [18]. Since both Fe atoms of the formula unit are electrochemically active, two electrons and two alkali ions can be transferred and inserted into BG, leading to a high theoretical specific capacity of 200 mAh g^{-1} relative to $Fe[Fe(CN)_6]$, which is equivalent to 171 mAh g^{-1} for $Na_2Fe(CN)_6$ (see Table S1) [12, 13]. The arrangement of the atoms, the fcc lattice with a perovskite-like structure, and the open diffusion pathways remain the same in BG as in the well-known PB [22].

In this study, we chose the promising BG as an electrode material and assemble cells with Li, Na, and K in order to evaluate the compatibility of BG with different monovalent insertion ions and to compare the electrochemical performance, electrode morphology, and stress evolution of BG with these ions during cycling. Although BG is not typically used as a positive electrode in metal-ion batteries due to the lack of alkali ions, its ability to accommodate various monovalent ions, such as Li^+, Na^+, and K^+ ions, makes it ideal for studying ion-specific effects. Given the distinct properties of these ions, we expect their interaction with shared electrode materials to result in different electrochemical, morphological, and mechanical responses. We investigate the influence of Li^+, Na^+, and K^+ ions on the performance and reliability of BG, using electrochemical measurements, intermittent scanning electron microscopy (SEM), and *operando* substrate curvature measurements. While keeping the same BG working electrode, we exchange the counter electrode and electrolyte during the experiments. Using this experimental strategy, we eliminate effects due to variations in electrode-related parameters and guarantee direct comparability of the results of BG with the different alkali ions and provide insights into ion-specific effects in positive electrodes.

2 | Experimental Section

2.1 | Material Synthesis

The active material of the positive electrode was BG, synthesized according to the description of Chen et al. [23]. XRD data of the as-synthesized powder are given in Figure S2 and confirm the expected cubic structure of BG. Table S3 shows data of elemental analysis (ICP-OES). The positive electrodes were composed of 80 wt% BG material, 10 wt% Super C65 carbon black (C65, Imerys Graphite & Carbon), and 10 wt% polyvinylidene fluoride (PVDF, Kynar HSV 900, Gelon Lib) and had a thickness of 120 µm. The electrode material was applied on an Al current collector with a carbon coating. The mass loading and active mass loading of the electrode materials within the film was about 3 and 2.4 mg cm^{-2}. The positive electrodes were dried at 100°C in a vacuum overnight.

The electrolyte solutions were prepared in an argon (Ar)-filled glovebox (MBraun) with water and oxygen content lower than 0.5 ppm. The electrolytes prepared and used were 0.75 M $LiPF_6$ in EC/DEC, 0.75 M $NaPF_6$ (Alfa Aesar) in EC/DEC (Sigma Aldrich), and 0.75 M KPF_6 (Alfa Aesar) in EC/DEC (Sigma Aldrich) with solvent ratios of 1:1. The electrolyte used in Li-ion cells was prepared by diluting a commercially available solution of 1 M $LiPF_6$ in EC/DEC (1:1) from Sigma Aldrich with EC/DEC (1:1) solvent. To ensure reasonable comparability between the Li, Na, and K cells, the electrolytes were chosen to be similar.

2.2 | Cell Preparation

2.2.1 | Assembly of Swagelok Cells

For the electrochemical characterization and SEM investigations, the BG electrodes were assembled into Swagelok-type cells. All measurements were carried out in half-cells with a two-electrode setup. The stainless steel cell parts were dried at 100°C and assembled in an Ar-filled glovebox. The Swagelok-type cell consisted of an electrode stack and a spring between two rods in a fitting. Teflon seals were located between the fitting and the rods, and the electrode stack was insulated from the metal housing by a perfluoroalkoxy alkane (PFA) tube. The BG electrode was used as working electrode and a metal disc as counter electrode.

Both counter and working electrodes had a diameter of 11 mm and were separated by a vacuum-dried 12 mm glass fiber separator (Whatman GF/B). For SEM, a cellulose separator (Nippon Kodoshi Corporation) with a diameter of 11 mm was placed between the working electrode and the glass fiber separator. For the investigation of Li^+, Na^+, or K^+ ion insertion, pure Li, Na, or K metal foils (all from Alfa Aesar) were rolled and cut into a disc and placed on a Ni current collector. The cells were then filled with 100 µL of electrolyte (0.75 M $LiPF_6$ in EC/DEC, 0.75 M $NaPF_6$ in EC/DEC or 0.75 M KPF_6 in EC/DEC) corresponding to the metal counter electrode.

2.2.2 | Assembly of Substrate Curvature Cells

To record mechanical stresses in materials, especially in thin films, *operando* curvature measurements were performed in dedicated substrate curvature cells. All cells were assembled in an Ar-filled glovebox. The general experimental setup follows that described by Schäfer et al. [24]. Three-electrode cells were used. For the counter and reference electrodes, pure metal was applied to Ni current collectors on stainless-steel plates. The working electrode was glued on a borosilicate glass cantilever with a thickness of about 155 µm and measuring about 15×4 mm. To enhance reflectivity, the back of the glass was sputter-coated with 30 nm of tungsten (W). In the curvature setup, the cell was fixed in place by clamps, enabling the removal and reinsertion of the cell without changing its initial position. Therefore, the cantilever and the laser spots on its surface keep their position, even after taking the cell out of the setup for the ion exchange and reinserting it. The ability to do so allows accurate comparison of the mechanical response of BG with the different insertion ions. A schematic drawing of the setup is shown in Figure 1. The curvature of the cantilever and the angle of the incoming beam are strongly exaggerated.

As the cantilever is curved by its changing stress distribution caused by volume changes during cycling, the position of the reflected laser spots on the camera and the distance between them change. The radius of curvature of the cantilever can therefore be determined by recording the position of the laser spots on the camera. The PVDF binder causes a drift in the curvature data that is not related to the electrochemical experiment and probably originates from its swelling in the electrolyte solvent. Therefore, this drift was manually corrected (subtracted) from the curvature data. The calculation of the stress variations from the displacement of the reflected laser beam is described by Choi et al. [25] Since the BG electrodes are thick (>100 µm), Stoney's relation [26] (derived for the condition $h_f \ll h_s$, with h_f and h_s being the thickness of the film and the substrate) is not directly applicable. Nevertheless, it can be assumed that the stress in the electrode is proportional [25] to the reciprocal radius of curvature, which we report in our datasets.

2.3 | Materials Characterization

The electrochemical cells were cycled at room temperature using a VMP3 multichannel potentiostat/galvanostat (Bio-Logic SAS). For each alkali metal, we performed one cycling stability test and one long-term electrochemical measurement combined with intermittent SEM. In addition, ion exchange experiments, carried out on cells assembled with the same single electrode, were combined with intermittent SEM measurements. During such an ion exchange experiment, the same electrode was cycled successively against different metal counter electrodes. For BG, the insertion/extraction of all three metal ions, i.e., Li, Na, and K, into/from the same electrode sample was observed. Thus, we performed two ion exchanges in combination with SEM: one BG electrode was successively cycled against Li, Na, and K, and another BG electrode was successively cycled against K, Na, and Li. In general, the galvanostatic measurements of BG were performed between 2.0 and 4.0 V versus Li^+/Li and versus Na^+/Na and between 2.5 and 4.0 V versus K^+/K.

We conducted microscopic characterization for the three electrodes of the long-term measurements and the two electrodes of the ion exchanges using a SEM (Zeiss Merlin FESEM). The SEM images were typically recorded at a working distance of 3 mm and an accelerating voltage of 3 kV. By employing intermittent SEM, morphological changes at identical positions within the electrode were observed and compared across different states of charge [27] and after ion exchanges. Acquiring SEM images of the exact same electrode location relies on larger irregularities on the sample surface that are observed at smaller magnifications

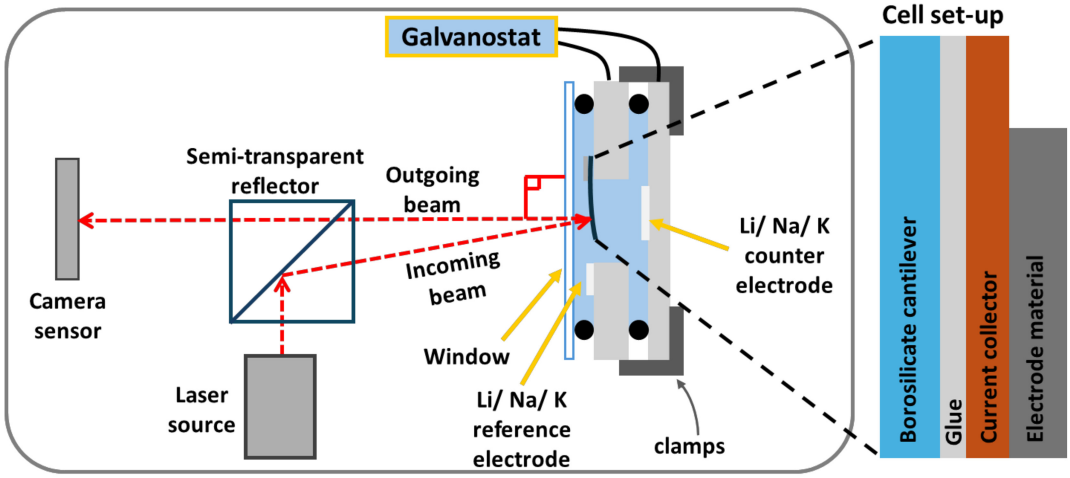

FIGURE 1 | Schematic image of the substrate curvature setup with the curvature cell on the right side (adopted and modified from [25]).

and can be used to navigate to the regions of interest in their vicinity. For SEM, the Swagelok cells were disassembled, and the electrodes were washed with DEC in order to remove residues of the electrolyte. The transfer into the SEM was performed under argon, preventing reactions of the materials with air. After imaging, the electrodes were mounted back into the Swagelok cells, and the electrochemical experiments were continued.

We further designed experiments to observe the impact of ion exchanges on *operando* substrate curvature measurements of BG. During the curvature experiment, we cycled the same BG electrode successively against Li, Na, and K at room temperature (20°C). Before exchanging the insertion ions, the reference electrode was electrochemically dissolved. The cell was then disassembled, washed with DEC to remove salt residues from the electrolyte, and the next metal counter and reference electrodes were inserted. The cantilever remained fixed so that the insertion/extraction of different ions into/from the same electrode could be observed without any readjustment of sample positions.

The term BG-AM (for example, BG-Li) is used to describe the cycling of BG against an alkali metal (AM = Li, Na, or K). The abbreviations BG//LNK and BG//KNL are used for the ion exchanges from Li to Na to K and vice versa.

3 | Results

We present a comprehensive electrochemical and morphological characterization of 12 cells, including two ion exchange experiments, with BG cycled against Li, Na, and K to elucidate the impact of different alkali metals on cycling performance and electrode morphology. To complement these investigations, we monitored the mechanical stress response of BG during ion exchange experiments involving sequential insertion and extraction of Li^+, Na^+, and K^+ ions. Electrochemical measurements were conducted between 2.0 and 4.0 V against Li^+/Li and Na^+/Na, and between 2.5 and 4.0 V against K^+/K. The tested half-cells consisted of BG as working electrode and either Li, Na, or K metal as the counter electrode. The electrochemical state of the working electrodes after charge and discharge corresponds to their delithiated/desodiated/depotassiated and lithiated/sodiated/potassiated states.

3.1 | Electrochemical Measurements

To investigate the cycling stability of BG, long-term galvanostatic measurements were carried out with half-cells. Figure 2a–c shows the specific discharge capacity and the Coulombic efficiency for each cycle for the cells assembled with Li, Na, and K as counter electrodes. Figure 2d–f displays the corresponding incremental capacities (IC) for each cell. For the BG-Li and BG-Na cells, we increased the specific current from 10 to 20 mA g^{-1} after 50 cycles (see dashed lines in Figure 2a,b), while keeping it at 10 mA g^{-1} for the cell with the K counter electrode in Figure 2c. Therefore, to allow comparison between the three cells, dQ/dV curves are presented only up to 50 cycles.

BG cells assembled with Li and Na displayed much higher cycle life (stopped after 450 cycles) than the cell with a K counter electrode (failed after 120 cycles). However, this K cell delivers the highest specific discharge capacities of BG of about 40 mAh g^{-1} over almost 120 cycles. Specifically, the first cycle displays a specific capacity of 64 mAh g^{-1} (Figure 2c). Nonetheless, rapid failure occurs in the BG-K cell after nearly 120 cycles, where the specific discharge capacity drops abruptly to a value close to zero. The BG-Li and BG-Na cells have similar electrochemical performance: Within the first 50 cycles, the discharge capacity decreases from approximately 40–28 mAh g^{-1}. Thus, after 50 cycles, around 70% of the initial specific discharge capacity remains. With Li, BG retains approximately 90% of the capacity between cycles 50 and 450. In all three cells (Figure 2a–c), low specific capacities are achieved, compared to the theoretical specific capacity of BG of 200 mAh g^{-1}. After the initial capacity decrease, the specific discharge capacities remain relatively stable over 400 cycles with a maximum decrease of only 5 mAh g^{-1}. Except for the first few cycles in the Na and K cells, all three alkali metals lead to Coulombic efficiencies of more than 90% over the course of the experiments. In the case of Na and K, the efficiency increases from around 92% to 97% during electrochemical cycling (Figure 2b,c). In particular, the cycling of BG with Li results in a steady Coulombic efficiency of 99% during the entire measurement.

The IC curves in Figure 2d–f show characteristic peaks with all cells exhibiting two distinct redox peaks (marked with (1) and (2)). The BG-Na cell displays dQ/dV peaks at higher potentials of approximately 45 (charge) and −50 mAh gV^{-1} (discharge), compared to approximately 25 (charge) and −25 mAh gV^{-1} (discharge) for the BG-Li cell at similar potentials. Both cells, however, exhibit a flattening of the IC curves with increasing cycle number. Especially the BG-Li cell shows indistinct plateaus and potentials above 3.2 V (Figure 2d). The IC curves corresponding to the BG-K cells in Figure 2f differ substantially from those of BG-Li and BG-Na. The peaks are sharper, closer together, and are shifted to potentials about 0.3 V higher than those of BG-Li and BG-Na cells (Figure 2d,e). These redox peaks appear in a potential range of 3.2–3.5 V during discharge, and between 3.4–3.6 V during charge. In contrast, the BG-Li and BG-Na cells display discharge and charge peaks in between 2.7–3.6 and 2.9–3.7 V. Over repeated cycling, the peaks of BG-K shift to higher potentials during charging and to lower potentials during discharging. Compared to the BG-Li and BG-Na cells (Figure 2d,e), the features are still very distinct even after 50 cycles (Figure 2f). During discharge, dQ/dV reaches zero at a potential of 3.1 V for BG-K. However, approaching the upper potential limit of 4.0 V, BG-K exhibits an increase in dQ/dV, whereas dQ/dV reaches zero in the BG-Li and BG-Na cells.

3.2 | Intermittent SEM During Long-Term Measurements

We present morphological investigations for three half-cells, in addition to the electrochemical characterization reported above. These cells were subjected to long-term electrochemical cycling and intermittent SEM, meaning that the working electrode was microscopically investigated at different electrochemical states and cycles. While the first cycle for each cell was recorded at 5 mA g^{-1}, the following cycles were carried out at 10 mA g^{-1}. The BG-Li and BG-Na cells were stopped after 300 and 280

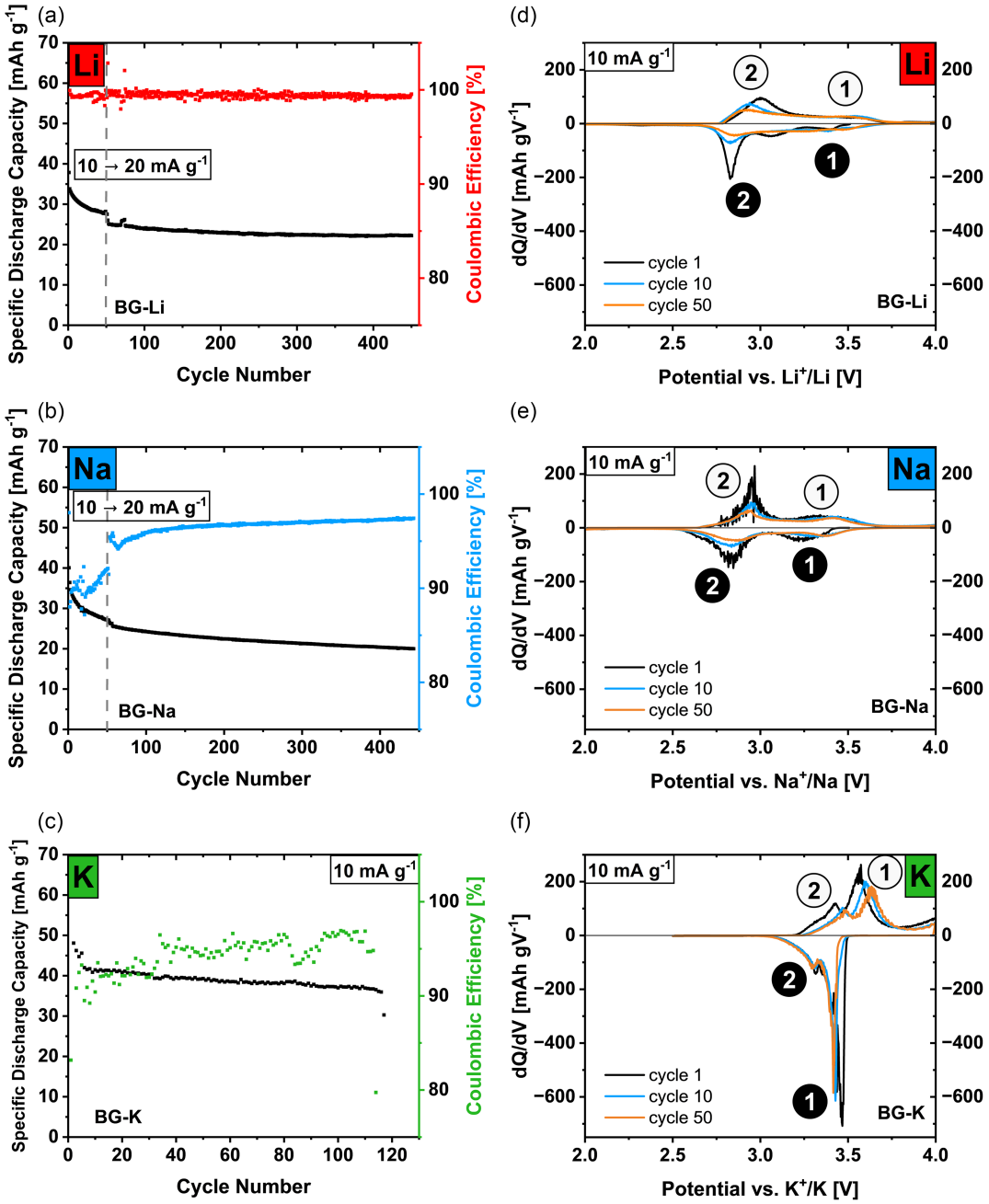

FIGURE 2 | Cycling stability and Coulombic efficiency of BG cycled against (a) Li with 0.75 M LiPF6 in EC/DEC between 2–4 V, (b) Na with 0.75 M NaPF6 in EC/DEC between 2–4 V, and (c) K with 0.75 M KPF6 in EC/DEC between 2.5–4 V. IC curves of BG cycled against (d) Li with 0.75 M LiPF6 in EC/DEC between 2–4 V, (e) Na with 0.75 M NaPF6 in EC/DEC between 2–4 V, and (f) K with 0.75 M KPF6 in EC/DEC between 2.5–4 V. For each cell cycles 1, 10, and 50 are presented.

cycles. The BG-K cell failed after approximately 120 cycles. The galvanostatic discharge/charge curves of the cells are shown in the supplementary materials in Figure S4 and show the similarity of BG with Li and Na and the overall higher potential of BG with K, as described above.

Figure 3 presents surface morphology changes of electrode (Figure 3a–c) and particle level (Figure 3d–f) of BG cycled against Na. The images in Figure 3a–c were acquired at the same location of the electrode in different electrochemical states: (a) in the discharged, i.e., sodiated and (b) charged, i.e., desodiated state of the first cycle, and the (c) discharged state after 280 cycles, i.e., sodiated, after the measurement was stopped. The images in Figure 3d–f show a different location on the same electrode in (d) the discharged and (e) charged state of the first cycle, and (f) the discharged state after 280 cycles.

The defects of the electrode are only apparent at a larger scale at the electrode level and not within individual electrode particles. We recorded a pre-existing crack/gap between the particles at the electrode level (seen in Figure S5a), which shows narrowing or widening during sodiation and desodiation (Figure 3). This fluctuation in the width of the cracks is highlighted by yellow arrows in Figure 3a–c. Since the BG electrode

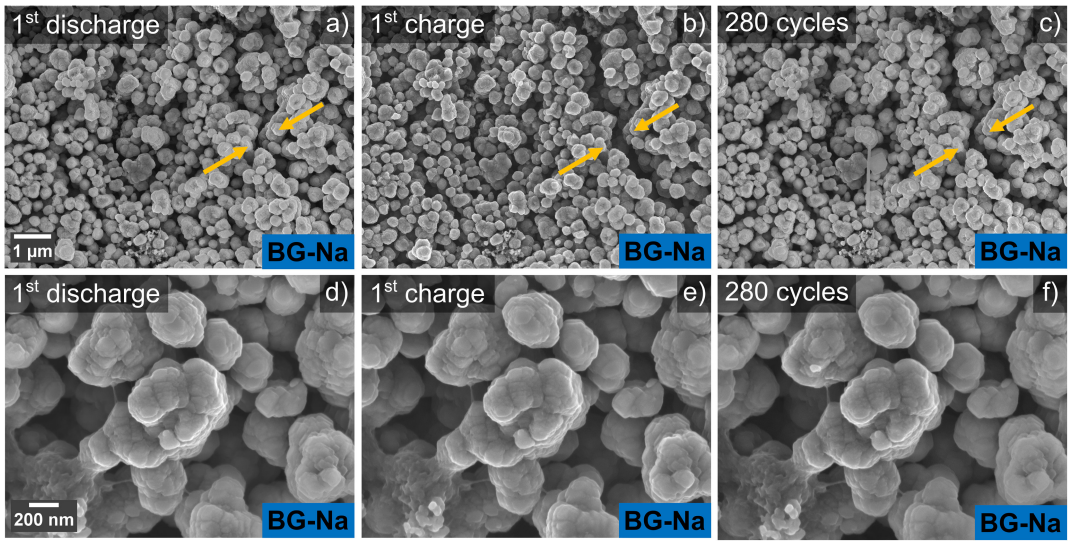

FIGURE 3 | SEM images of a BG electrode cycled against Na (BG-Na) with 0.75 M $NaPF_6$ in EC/DEC between 2–4 V in different electrochemical states: (a,d) after 1st discharge, (b,e) after 1st charge, and (c,f) after discharge after 280 cycles. Images (a–c) and (d–f) depict different positions on the same BG electrode at different magnifications.

was discharged (sodiated) after 280 cycles, the corresponding SEM image should be compared with the image of the first discharge. After 280 cycles, Figure 3c shows minor growth of the crack in the sodiated BG electrode compared to the sodiated state of the 1st cycle. We observed similar changes between the charged and discharged states, and during cycling, for the BG electrodes cycled against Li and K. At the particle level, no detectable changes, such as crack formation and growth or significant volume changes, appear in all three cells, as shown in Figure 3d–f by the example of the BG-Na cell. In all three cells, apart from pre-existing cracks, the morphology of large investigated areas of the electrodes did not change despite 300, 280, and 120 cycles, showing no crack formation or strong irreversible volume changes, either at the electrode or at the particle level. Notably, in the cell with K as the counter electrode, a significant expansion of pre-existing electrode cracks is apparent at a larger scale already after approximately 120 cycles (see Figure S6).

3.3 | Ion Exchange in the Same BG Electrode: Electrochemistry and Morphology

For a direct comparison of the behavior of BG with different monovalent insertion ions, the same individual electrodes were cycled subsequently against Li, Na, and K metal. This experimental strategy to investigate the ion exchange allows to probe the stability and reversibility of the BG for ions of different size. Using intermittent SEM, we compared the morphological changes after ion exchange and the effect of different alkali ions on electrode degradation.

Figure 4 depicts the electrochemical measurements of the BG cells containing different ions. In Figure 4a, we present the electrochemical characterization of the same BG electrode assembled with alkali metals in increasing order of ionic radius ($Li^+ < Na^+ < K^+$). This order is referred to as BG//LNK. In Figure 4b, we present the electrochemical characterization of another BG electrode assembled with alkali metals in reverse order, thus in decreasing order of ionic radius ($K^+ > Na^+ > Li^+$). This order is referred to as BG//KNL. In both cases, the electrode was cycled for one cycle against each metal at 10 mA g^{-1}. Holding steps at a potential of 4.0 V were added in some experiments in order to ensure complete extraction of the alkali ions from the electrode before inserting the next metal ion. Comparing both Figure 4a,b, higher specific capacities of around 60 to 70 mAh g^{-1} for all three ions are reached when Li is inserted into the electrode first. In contrast, only capacities of approximately 40 to 50 mAh g^{-1} are achieved when K is used first, except for the first charge of the cell. In both BG//LNK and BG//KNL sequences, the BG-Li and BG-Na cells consistently show a very similar potential curve. Similar to the dQ/dV data in Figure 2, the potential of the BG-K cells is shifted to values significantly higher than that for Li and Na.

In addition to the electrochemical data of the BG//LNK and BG//KNL cells depicted in Figure 4, we recorded morphological changes using intermittent SEM. We carried out these investigations prior to the first electrochemical measurement and after each individual cycle, i.e., when the insertion ions were exchanged and assume that all insertion ions were removed from the electrode at the end of each cycle. For this purpose, all cells were disassembled after each cycle, and the BG working electrode was examined by SEM before changing to the next alkali metal. Thus, the electrodes were examined after the complete extraction of ions. The SEM images corresponding to the data presented in Figure 4a,b are shown in Figures S7 and S8, respectively. For all cells, we observed little to no changes in the electrode due to cycling with the different ions. Cracks that form within the first cycle with Li or K do not increase in length, nor do the gaps widen (Figures S7 and S8). In addition, the amount of Na and K in the BG electrode within the BG/KNL cell is shown in the energy-dispersive X-ray spectroscopy (EDX) data in Table S9 in the supplement. As with the SEM images of the ion exchange at the electrode level, no significant differences are observed at the particle level either (Figure S10). The only change recorded with SEM is that the surface features become

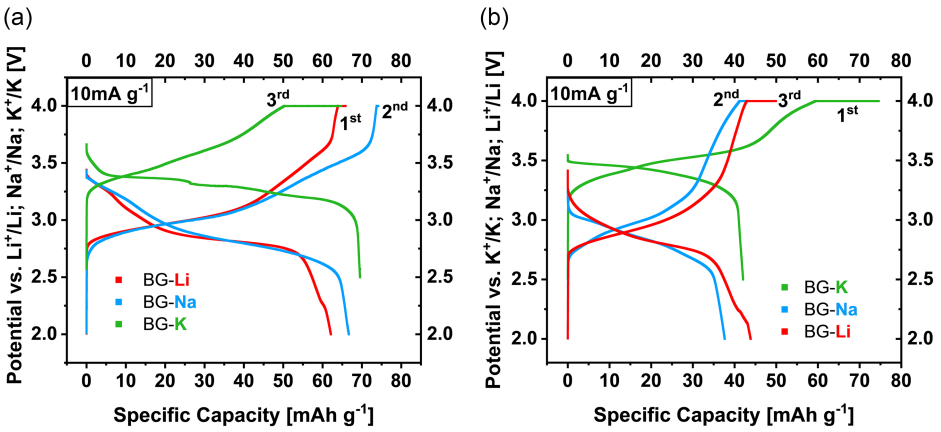

FIGURE 4 | Galvanostatic discharge/charge curves of the (a) BG//LNK cell and the (b) BG//KNL cell. For each cell, BG is cycled against Li with 0.75 M $LiPF_6$ in EC/DEC between 2–4 V, against Na with 0.75 M $NaPF_6$ in EC/DEC between 2–4 V, and against K with 0.75 M KPF_6 in EC/DEC between 2.5–4 V.

more rounded and softer during cycling. These changes happen during the first cycle but are equally pronounced for the different insertion ions.

3.4 | Ion Exchange in the Same BG Electrode: Mechanical Stress During Galvanostatic Cycling Against Li, Na, and K

We investigated the evolution of the mechanical stress in BG during operation, using the same strategy of ion exchange in cells assembled for substrate curvature measurements, with the exchange conducted in order of increasing ionic radius. With each metal, the cell was cycled for three cycles at a specific current of $3\,mA\,g^{-1}$. Before exchanging the counter electrode, and therefore the insertion ion, the reference electrode was electrochemically fully dissolved to avoid traces of the previously used metal in the cell. Figure 5 shows the curvature (reciprocal radius of curvature) of the BG cantilever over time, along with the cell potential for BG//LNK, with separate diagrams displaying the data for the individual insertion ions in the same electrode. The curvature is proportional to the stress that forms due to electrochemical cycling [25]. Curvature values above/below zero indicate a shift toward tensile/compressive stresses relative to the initial state of the cantilever. The general trends in the data are very similar for BG-Li and BG-Na (compare Figure 5a,b). Both show the same characteristic features throughout all three cycles: distinct negative (compressive) peaks at the potential of 2 V and two tensile maxima near (but not at) the potential of 4 V. However, the curvature amplitudes for BG-Na are almost twice as large as those of BG-Li, with values up to $0.03\,m^{-1}$ compared to $0.015\,m^{-1}$ for BG-Li. In addition, a larger curvature can be observed in the data of BG-Na when the potential is reversed at 4 V. Compared to the smaller Li^+ ions, the change from extraction to insertion of the ions (around 4 V) and vice versa has a greater effect on the shape of the curve for Na^+ ions. In general, relative to the initial state of the cantilever, BG is predominantly in the negative curvature range (compression) for both alkali ions. For lithiation, however, the curvature shifts to positive values at higher potentials. This can be observed in all three cycles, whereas no shift into the positive range can be observed for BG-Na compared to the initial state of the cantilever.

Figure 5c presents curvature data for the BG-K cell in the BG//LNK order and shows key differences with previous cells. These differences underpin the distinct behavior of potassium in the electrochemical data of Figure 2. In contrast to Li and Na, the BG electrode stays consistently under tensile stress throughout the three cycles against K. Irrespective of the sign of the stress, the stress amplitudes for BG-K are approximately three and six times lower than the respective amplitudes for BG-Li and BG-Na. Unlike BG-Li and BG-Na, the peak in the stress corresponding to the lower potential limit (2.5 V for BG-K) is significantly less sharp. The potential profile in Figure 5c remains consistent across all three cycles, showing two sloping regions around 3.9 and 3.1 V. In the curvature data, in contrast to the maxima in Figure 5a,b, minima appear, associated with the sloping region in the potential at approximately 3.2 V. The change in direction of the curvature occurs near the mid-potential range rather than close to the upper potential limit, especially compared to BG-Li.

4 | Discussion

In this study, we present electrochemical, morphological, and stress measurements on BG electrodes cycled against Li, Na, and K metal. We demonstrate that (1) BG enables highly reversible insertion of Li^+, Na^+, and K^+ ions, (2) associated volume changes are largely reversible, and morphology changes are similarly small for all three ions, and (3) K^+ ions lead to different behavior in BG compared to Li^+ and Na^+ ions. In the following section, we discuss the reliability and versatility of BG with different alkali metals, examine its distinct behavior caused by the different alkali ions, and consider the broader implications of our findings for the use of BG in future battery technologies.

4.1 | The Electrochemical Impact of Different Alkali Ions on BG

We present long-term electrochemical measurements to highlight the reversible ion insertion into BG and to evaluate its stability for Li^+ ions and beyond. We confirm a high reversibility of the

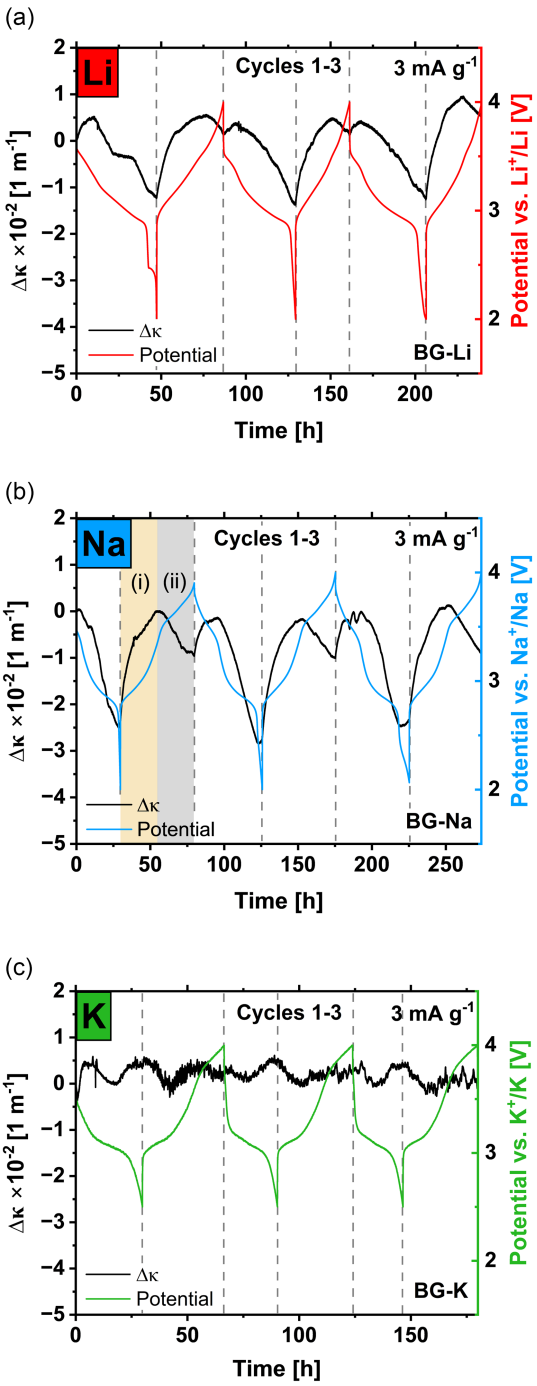

FIGURE 5 | Curvature of the BG cantilever and corresponding potential profiles plotted over time during galvanostatic cycling in the BG//LNK ion exchange setup. Shown are measurements of BG against (a) Li with 0.75 M $LiPF_6$ in EC/DEC between 2–4 V (cycles 1–3), (b) Na with 0.75 M $NaPF_6$ in EC/DEC between 2–4 V (cycles 4–6), and (c) K with 0.75 M KPF_6 in EC/DEC between 2.5–4 V (cycles 7–9).

capacity of BG electrodes with Li, Na, and K, similar to published literature [14, 21, 28], with high Coulombic efficiencies of BG cycled against Na and K, and the steady Coulombic efficiency of 99% against Li (Figure 2a–c). In Figure 2a, BG cells demonstrate approximately 90% capacity retention over 400 cycles with lithium, similar to the results obtained by Shen et al. with around 70% of specific capacity remaining after 50 cycles against Li with 1 M LiPF6 in EC/DMC (1:1) [29]. Such cyclability of BG with Li was also observed by Wu et al. with a low defect $FeFe(CN)_6$ material [28]. In Figure 2, the half cycles consumed between 1 and 4 h. These high rates could contribute to kinetic limitations and, therefore, to the observed low specific capacities in all three cells compared to the theoretical capacity of BG. It should be emphasized that due to the low capacities, BG cannot be considered suitable for practical Li-batteries and batteries beyond Li at this stage. The scope of this work is instead directed toward the fundamental understanding and the comparison of ion insertion into BG. Several factors can explain the reduced capacities observed, such as imperfections during material synthesis and incomplete reactions [30, 31]. For example, according to Shen et al. [29], the incomplete extraction of K^+ ions from $K_3Fe(CN)_6$ during the synthesis of the electrode material could lead to residual Fe^{II} present in the structure and lower the achievable capacity [29]. It is important to note that $Fe(CN)_6$ vacancies can impact the structure, stability, and performance of the electrode [28, 32, 33]. The coordinated water within the vacancies breaks down the Fe–CN–Fe bridging, leading to a distorted and structurally unstable lattice [32, 34, 35]. Furthermore, the coordinated water can block channels for ion transport and redox-active sites, decreasing the number of available sites for insertion ions and, therefore, reducing the capacity [21, 33, 36, 37]. The observed low capacities of around 40 (Figure 2) to 70 mAh g^{-1} (Figure 4) may relate to the drying under vacuum at a temperature of 100°C. According to the literature, by raising the drying temperature to 150°C, the specific capacity can be increased by roughly 50% [38]. Nevertheless, these increased capacities are still far below the theoretical specific capacity, and such improvements cannot compensate for the structural limitations of the material and the resulting capacity losses and further optimization would be necessary. In our elemental analysis in Table S3, we identify small amounts of K, indicating an incomplete extraction during synthesis, and lower Fe contents than expected, which is probably related to $Fe(CN)_6$ vacancies. Even highly optimized PBA electrodes typically deliver around 100–160 mAh g^{-1}, considerably below the theoretical capacity [14, 21, 28, 39–41]. Independent of the water content, $Fe(CN)_6$ vacancies impact the electronic conduction pathways in the framework, resulting in an impeded insertion reaction of the alkali ions in the respective areas [20]. Therefore, the presence of lattice defects and water results in low specific capacity, low efficiency, and generally deteriorated electrochemical performance of PBAs [32]. During electrochemical cycling, the water molecules could enter the electrolyte and undergo electrochemical decomposition, causing a deterioration of the organic electrolyte, reducing the concentration of effective ions for transport, and affecting the degradation of the battery [18].

The characteristic IC peaks in Figure 2d–f are equivalent to plateaus in the potential profiles and correspond to phase transitions in the active materials induced by the insertion/extraction of ions. The transition from BG to PB corresponds to the redox flip of C-coordinated low-spin (LS) Fe ion (LS $Fe^{3+/2+}$–C) units and to the peak at higher potential and the subsequent transition from PB to PW corresponds to the redox flip of N-coordinated high-spin (HS) Fe ion (HS $Fe^{3+/2+}$–N) units and to the peak at the lower potential [42]. Although the achieved specific capacities are lower than the theoretical value, the electrochemical profiles obtained from the dQ/dV data (Figure 2d–f) exhibit characteristics consistent with those reported for high-capacity BG electrodes: The redox peaks at

around 2.8/3.1 and 3.3/3.5 V for BG-Li and BG-Na resemble those reported for LIB (2.7/3.1 and 3.4/3.9 V [29] and SIB (2.78/3.10 and 3.47/3.74 V) [21]. During cyclic voltammetry of BG against K, Shadike et al. [14] observed oxidation/reduction peaks at 3.4/3.2 and 3.6/3.4 V, which show strong similarity with our observations in Figure 2f. These similarities indicate that the relevant electrochemical processes are captured in our measurements, enabling our analysis of ion-dependent phenomena. We suggest that the similar electrochemical behavior and dQ/dV signals of BG-Li and BG-Na, contrasted by the distinct response of BG-K, indicate different insertion/extraction mechanisms for K. Other studies have already reported that BG electrodes exhibit distinct electrochemical behaviour when cycled against K compared to Li and/or Na. These differences have been attributed to (i) ion insertion into different BG lattice sites and (ii) differences in electronic interactions with the host structure.

(i) Based on Raman and XRD measurements, Li et al., observed different reaction pathways for BG electrodes cycled against Na and K, accounting for the different potentials [43]. Moreover, in simulations of Ling et al. large cations prefer to occupy the body-centered site of $FeFe(CN)_6$, while small cations prefer to occupy the face-centered site with a shorter cation–anion bonding distance. In this way, ions with larger ionic radius intercalate at higher voltages [44].

(ii) Heo et al. observed an upshifting of the equilibrium working potentials of the LS Fe–C and HS Fe–N units for BG in KIB cells compared to LIB and SIB cells and explained it by differences in the interaction between the alkali ion and the CN group [42]. Our peak shift for BG-K in Figure 2f is consistent with the observations/mechanisms (i) and (ii), and a clear distinction cannot be made based on electrochemical data.

Comparing the IC curves of all three cells (Figure 2d-f), significant flattening occurs with increasing cycle number, indicating that less charge is involved in the processes and reactions taking place due to either a loss of BG active material during electrochemical cycling against Li and Na or due to the blocking of insertion ions. The observed shift of the peaks of BG-K to different potentials may be caused by an increasing resistance, e.g., by the formation of an anodic or cathodic SEI layer on the active materials, causing an additional overpotential. In contrast to BG-Li and BG-Na ($dQ/dV = 0$), for BG-K, the dQ/dV signal increases at the upper potential limit. We suggest that the potential increase indicates electrolyte decomposition at high voltages, which may be reflected in the lower Coulombic efficiency for BG-K, compared to BG-Li and BG-Na. K shows high reactivity and decomposes the carbonate-based electrolyte [45]. The decomposition products can lead to crosstalk, resulting in irreversible currents at higher voltages [46].

4.2 | Morphology Changes in BG with Different Alkali Ions

The morphological changes between the charged and the discharged states are similar for Li^+, Na^+, and K^+ ions and can be attributed to the repeated insertion and extraction of the alkali ions. These fluctuations, reflected in reversible crack expansion, indicate stability of the BG electrodes toward repeated cycling with all three alkali species. The associated volume changes are linked to periodic mechanical stresses and lattice strains during ion insertion and extraction (see Figure 5). However, the extent of these volume fluctuations over long-term cycling is significantly smaller than those within a single cycle: The comparison of the corresponding states (e.g., Figure 3a,c) shows minor growth of the crack after extended cycling over 280 cycles, demonstrating that BG can tolerate repeated volumetric changes with little mechanical degradation. The crack visible in Figure 3 was already present in the pristine electrode (Figure S5a) and originates from drying during the electrode preparation. These drying cracks on the electrode level show the most widening after cycling for BG-K (Figure S6d). After the failure of the cell (BG-K in Figure S6d), a new BG-K cell was assembled with the same BG electrode and cycled for another 40 cycles until failure (Figure S6e). We suggest that in this cell, the K-metal electrode was not reliable and that the pre-existing crack in the BG electrode played a minor role. The origin of mechanical stress of a composite electrode is mostly governed by the volume change of the active material, which causes stresses in the passive components [47]. In the active particles, the stress depends on the reaction pathway and does not necessarily correlate with their volume changes and the stresses measured at the level of the composite electrode [48]. Therefore, a separate consideration of stresses in the composite electrode and in individual active particles is useful.

At the level of individual particles (Figure 3d-f), we do not detect changes such as crack formation and growth or significant volume changes. Heo et al. also concluded that BG can effectively serve as a host framework for accommodating and releasing Li^+ and Na^+ ions without structural breakdown [42], which is consistent with our results. Our findings demonstrate that BG is a very stable material with good lattice integrity and reliability, due to the stability of the particles against significant crack formation and volume changes [28].

4.3 | Ion Exchanges Do Not Induce Damage of the BG Electrodes

We used intermittent SEM to correlate the electrochemical measurements and surface morphology of the same BG electrode cycled against different alkali metals in two experimental routines, including exchanges of the counter electrode, BG//LNK and BG//KNL. The SEM observations (Figures S7 and S8) associated with the electrochemical measurements in Figure 4 show no morphological differences of the BG electrode throughout sequential cycling against three different alkali metals. These results and the relatively high Coulombic efficiencies of the half cells of approximately 85%–99% support the previously described findings that BG can reversibly incorporate the three different alkaline ions into its framework regardless of their size. EDX data (Table S9) show that the different metal ions can be extracted after each cycle.

In Figure 4b, lower capacities are present in the BG//KNL cell, i.e., when the ions are exchanged from the largest to the smallest, compared to the BG//LNK cell. An explanation for the reduced capacity for Li and Na in Figure 4b could be that insertion and extraction of K alters the host structure. A different explanation, namely that a K-containing CEI blocks Li^+ and Na^+ ions, seems

unlikely because this would lead to ohmic drops, i.e., increased potential of ion extraction and decreased potential during ion insertion, which we do not observe (cf. Li and Na data of Figure 4a and b). The morphological stability of the electrode for the different ions also suggests that the insertion of one metal ion is not strongly affected or blocked by an existing CEI that has formed earlier using a different ion.

Compared to Figure 2, the capacities in Figure 4 show some variation due to different electrode batches prepared in small quantities. Both batches display consistent electrochemical characteristics for the active material and thus permit direct comparison.

4.4 | Mechanical Stresses During Ion Exchange Using the Same BG Electrode

When comparing the curvature measurements of BG cycled against Li, and of the same BG electrode cycled against Na, the overall larger curvature amplitudes of BG-Na (BG//LNK, Figure 5a,b) are apparent. The larger range (the difference between minimum and maximum stress) indicates higher stresses in the electrode, which are probably due to the larger ionic radius of the Na^+ ions, generating larger volume changes within the electrode material and possibly causing structural instability [42, 49]. For both Li^+ and Na^+ ions, BG is mostly under compressive stress compared to the start of the measurements. While BG-Li periodically develops small tensile stresses, the BG-Na cell exhibits only compressive stresses.

However, BG-Li and BG-Na possess similar curvature profiles, as reflected by characteristic features such as the distinct negative stress peaks at the potential of 2 V and the two maxima near the potential of 4 V (compare Figure 5a,b). The reason for the similar trends might be the occupation of similar lattice sites within the BG lattice of the Li^+ and Na^+ ions. Through first-principles calculations (GGA + U), Ling et al. [44] showed that both the Li^+ and Na^+ ions are likely to occupy the 24d sites (face-center of the cubic lattice) and Baumgart et al. [50] also state the preference of Na to occupy the 24d position. For the largest parts of the curves in Figure 5a,b, the increase and decrease of compressive stresses in the electrode correspond to the insertion and extraction of the ions into/from BG. The change of the bond length of the HS Fe–N unit was observed by Heo et al. using EXAFS analysis, and it increased during discharging (ion insertion) and decreased during charging (ion extraction) [42]. This change aligns with the observed compression (increasing negative curvature), i.e., volume expansion, during the insertion process and the volume contraction (development of tensile stresses), after switching to extraction in Figure 5a,b. According to the studies of PB with Na by Baumgart et al., the variation in the Fe—N bond length is minimal between BG and PB, but significantly increases when the fully sodiated state (PW) is reached [50].

Volume changes and resulting mechanical stresses in BG are consequences of the reaction mechanisms. For both, BG-Li and even stronger for BG-Na, two maxima in the stress around 4 V can be distinguished. The formation of these maxima at constant current corresponds to a change of direction in the mechanical stress from tension to compression. This effect coincides with the change in slope observed in the potential curves and likely corresponds to a change in the underlying reaction pathway between two regions as exemplified in Figure 5b: In region (i), the voltage exhibits a steep, curved increase and the corresponding stress evolves nonlinearly toward tension. Such behavior may indicate a solid-solution reaction. In contrast, in region (ii), the behavior is quite linear in voltage and stress with an overall smaller change compared to region (i). Two-phase coexistence regions are commonly associated with a plateau in the voltage and a linear change in the volume/curvature. Here in (ii), the Na-rich phase (maximum in curvature) seems to exhibit a smaller volume than the Na-poor phase (minimum at 4 V), suggesting that this region (ii) may be associated with a two-phase reaction between these phases. The symmetry of the curves around the points of current reversal further implies symmetrical reaction pathways, i.e., comparable mechanism, arising during ion extraction and insertion, also highlighting the reversibility of the process. A similar symmetry was observed by He et al. [51]; Wu et al. observed two peaks at 2.8 and 3.5 V during cyclic voltammetry of BG with Na, indicating the transition of the two Fe atoms in the crystal from Fe^{II} to Fe^{III} [21]. These peaks correlate with the insertion of the alkali ions into BG. The presence of the alkali ions affects the atomic structure of the host lattice and induces distortion modes. Cattermull et al. explored the different distortion mechanisms in PBAs, including octahedral tilts as well as A-site occupancy and "sliding" [35]. Cooperative tilts of the $Fe(CN)_6$-groups are the origin of the transition between the cubic and the rhombohedral phase [35]. This insertion-induced phase transformation has been frequently reported for both Li^+ and Na^+ ions [18, 42, 52, 53].

In the curvature experiment of BG-K (Figure 5c), we observed clear differences compared to Li and Na: Our experiments reveal that the BG electrode shows mainly tensile stresses when cycled against K, while mainly compressive stresses are present for Li and Na. The curvature of BG-K shows opposite characteristics compared to BG-Li and BG-Na: The mechanical stress exhibits a maximum where the other ions lead to a minimum, and vice versa. Correspondingly, Li^+ and Na^+ ion insertion drives the curvature toward compression, whereas K^+ insertion shifts it toward tension.

The larger ionic radius of the K^+ ions could lead to increased lattice strain levels compared to Li^+ and Na^+ ions and, based on observations of lattice strain in the BG framework due to repeated insertion/extraction of ions, Heo et al. hypothesize that the lattice strain is more pronounced for insertion ions with larger ionic radii, such as K [42]. However, our experiments show that larger ionic radii do not necessarily induce larger volume changes in our electrode compared to smaller ions: We observed that the largest relative tensile stresses (~0.005 m^{-1}) determined for BG-K are about three and six times lower than the largest relative compressive stresses for BG-Li and BG-Na (~0.015 m^{-1} and ~0.03 m^{-1}). The low mechanical stresses in Figure 5c cannot explain the observed degradation of BG-K during long-term cycling (only approximately 120 cycles, see Figure S6), and this early degradation might instead be initiated by processes at the surface of the metallic K electrode.

The lower stresses observed for BG-K arise from different site occupation of the ions, with the K^+ ions preferentially occupying the 8c sites, whereas the Na^+ and Li^+ ions mainly insert into the 24d sites [44]. The different insertion site is established in the

literature and directly rationalizes the observed stress amplitudes. Liao et al. synthesized $Na_xK_yFe[Fe(CN)_6]$ and determined the lattice parameter during cycling [54]. They revealed that the PBA lattice contracts during insertion and expands during the extraction of K^+ ions. This agrees with our observation (Figure 5c) of tensile stresses (contraction of the electrode) during insertion. Liao et al. observed in their $Na_xK_yFe[Fe(CN)_6]$ that the K^+ ions occupy the 8c sites and that at higher Na^+ ion concentration, Na^+ ions are pushed into the lower-symmetry 24d sites, causing stronger local lattice distortions and larger macroscopic stresses. Despite the larger ionic radius, K^+ ion insertion reduces the lattice parameter and mechanical stress, acting as a structural stabilizer that counteracts Na^+-induced lattice distortions that are of opposite sign [54]. This site-dependent distortion behavior is in agreement with the broader picture established by Cattermull et al., in which only cations larger than Na^+ occupy the body-center of the nanopore (8c), while Na^+ can reside in the square windows (24d) of the anionic framework, interacting more strongly with the cyanide ligands and thereby promoting octahedral tilts rather than the slide distortions characteristic of K^+-rich systems [35, 55]. A mechanistic difference in the insertion between Li^+, Na^+, and K^+ ions is interstitial water, which can accompany the Li^+ and Na^+ ions but not the K^+ ions in the 8c sites [35]. The larger volume changes of our BG-Na electrode, compared to BG-K, is further supported by the review of Hosaka et al. [56], in which *operando* XRD studies show that KMnFe-PBA undergoes approximately 6% less volumetric change during cycling compared to rhombohedral NaMnFe-PBA [56, 57]. We conclude that K follows a different reaction pathway with different lattice parameters and phase transformations, resulting in a different mechanical response. This is consistent with the observed higher insertion potentials and in line with the mechanism (i), as discussed in the electrochemistry section before.

Overall, our findings demonstrate that the ionic radius is only one of several factors determining the mechanical and electrochemical stability of electrode materials as well as their suitability for emerging technologies, and that the insertion of larger ions does not inherently lead to stronger degradation or preclude the use of established materials.

5 | Conclusion

Although different alkali metal ions exhibit similar physical and chemical properties, their differing ionic radii imply varying behavior when used as insertion ions in electrode materials. In this study, we systematically compare the insertion and extraction of Li^+, Na^+, and K^+ ions with a PBA electrode. The investigation focuses on BG and explores the effects of these alkali ions on its electrochemical performance, electrode and particle morphology, and mechanical reliability. To achieve this, we used a combination of electrochemical measurements, intermittent SEM, and *operando* substrate curvature experiments. Furthermore, to directly assess the influence of each alkali ion on the same electrode material, we carried out ion exchanges during the electrochemical tests by replacing both the counter electrode and the electrolyte.

Overall, our experiments demonstrate that BG can reversibly accommodate each of the three alkali ions into its structure, regardless of its size, which allows the direct comparison within a single electrode. The selected ion seems to have no significant influence on the surface morphology of the active material. Although BG exhibits volume changes as a result of the insertion/extraction of alkali ions, these changes are largely reversible. On a macroscopic scale, i.e., with respect to cracks in the coating layer, the most pronounced effects have been observed with K. However, although the larger ionic radius of the K^+ ions is expected to lead to increased stress levels of BG compared to Li^+ and Na^+ ions, the measured mechanical response isweakest for K. The K^+ ions likely occupy different sites within the BG lattice, leading to distinct IC peaks and corresponding mechanical behaviour, which together indicate a different insertion mechanism compared to Li and Na. In contrast, Li^+ and Na^+ ions follow similar insertion mechanisms, yielding comparable potential profiles, cycling stabilities, and Coulombic efficiencies, along with similar characteristics of the mechanical stress evolution during cycling. However, Na^+ ion insertion leads to higher stresses in the in BG than Li^+ ions. In general, the electrochemical and structural performance of BG is similar for each of the alkali ions tested, and the processes are highly reversible. These findings highlight the ion-tolerant structure and reliability of BG across a range of alkali ions, underscoring its potential as a versatile electrode material. Since the BG framework does not provide alkali ions, it may specifically be a suitable electrode material for metal batteries and a model system for studying different ion insertion mechanisms. Enabling the reliable use of alkali metal electrodes in battery applications requires further optimization of electrolytes and interphases to ensure the reversible and reproducible deposition and dissolution of the different metals. Stable anode materials would help to improve the safety of K-based cells. Their combination with BG cathodes might develop into an environmentally friendly and cost-efficient alternative to today's battery technologies.

Acknowledgments

This work contributes to the research performed at CELEST (Center for Electrochemical Energy Storage Ulm-Karlsruhe). The authors acknowledge support by POLiS Cluster of Excellence funded by the German Research Foundation (DFG) under project ID 390874152.

Open Access funding enabled and organized by Projekt DEAL.

Funding

This study was supported by Deutsche Forschungsgemeinschaft (390874152).

Conflicts of Interest

The authors declare no conflicts of interest.

Data Availability Statement

The data that support the findings of this study are available from the corresponding author upon reasonable request.

References

1. D. Kundu, E. Talaie, V. Duffort, and L. F. Nazar, "The Emerging Chemistry of Sodium Ion Batteries for Electrochemical Energy Storage," *Angewandte Chemie International Edition* 54, no. 11 (2015): 3431–3448.

2. Y. Yang, J. Zhou, L. Wang, et al., "Prussian Blue and Its Analogues as Cathode Materials for Na-, K-, Mg-, Ca-, Zn- and Al-Ion Batteries," *Nano Energy* 99 (2022): 107424.

3. M. Dahbi, N. Yabuuchi, K. Kubota, K. Tokiwa, and S. Komaba, "Negative Electrodes for Na-Ion Batteries," *Physical Chemistry Chemical Physics* 16, no. 29 (2014): 15007–15028.

4. P. U. Nzereogu, A. D. Omah, F. I. Ezema, E. I. Iwuoha, and A. C. Nwanya, "Anode Materials for Lithium-Ion Batteries: A Review," *Applied Surface Science Advances* 9 (2022): 100233.

5. M. Fleming, S. G. Kannan, and R. Eggert, "Long-Run Availability of Mineral Resources: The Dynamic Case of Lithium," *Resources Policy* 97 (2024): 105226.

6. W. Zhang, Y. Liu, and Z. Guo, "Approaching High-Performance Potassium-Ion Batteries via Advanced Design Strategies and Engineering," *Science Advances* 5, no. 5 (2019): eaav7412.

7. V. Gabaudan, L. Monconduit, L. Stievano, and R. Berthelot, "Snapshot on Negative Electrode Materials for Potassium-Ion Batteries," *Frontiers in Energy Research* 7 :46 (2019): 1–16, https://www.frontiersin.org/journals/energy-research/articles/10.3389/fenrg.2019.00046/full.

8. Y.-H. Zhu, X. Yang, T. Sun, et al., "Recent Progresses and Prospects of Cathode Materials for Non-aqueous Potassium-Ion Batteries," *Electrochemical Energy Reviews* 1, no. 4 (2018): 548–566.

9. M. D. Slater, D. Kim, E. Lee, and C. S. Johnson, "Sodium-Ion Batteries," *Advanced Functional Materials* 23, no. 8 (2013): 947–958.

10. S. Komaba, T. Hasegawa, M. Dahbi, and K. Kubota, "Potassium Intercalation into Graphite to Realize High-Voltage/High-Power Potassium-Ion Batteries and Potassium-Ion Capacitors," *Electrochemistry Communications* 60 (2015): 172–175.

11. A. Eftekhari, Z. Jian, and X. Ji, "Potassium Secondary Batteries," *ACS Applied Materials & Interfaces* 9, no. 5 (2017): 4404–4419.

12. S. Chong, Y. Chen, Y. Zheng, et al., "Potassium Ferrous Ferricyanide Nanoparticles as a High Capacity and Ultralong Life Cathode Material for Nonaqueous Potassium-Ion Batteries," *Journal of Materials Chemistry A* 5, no. 43 (2017): 22465–22471.

13. G. He and L. F. Nazar, "Crystallite Size Control of Prussian White Analogues for Nonaqueous Potassium-Ion Batteries," *ACS Energy Letters* 2, no. 5 (2017): 1122–1127.

14. Z. Shadike, D.-R. Shi, T.-W. Tian-Wang, et al., "Long Life and High-Rate Berlin Green FeFe(CN) 6 Cathode Material for a Non-Aqueous Potassium-Ion Battery," *Journal of Materials Chemistry A* 5, no. 14 (2017): 6393–6398.

15. B. Wang, Y. Han, X. Wang, et al., "Prussian Blue Analogs for Rechargeable Batteries," *iScience* 3 (2018): 110–133.

16. H. J. Buser, D. Schwarzenbach, W. Petter, and A. Ludi, "The Crystal Structure of Prussian Blue: Fe4[Fe(CN)6]3.xH2O," *Inorganic Chemistry* 16, no. 11 (1977): 2704–2710.

17. X. Xu, S. Zhu, C. Yang, et al., "A Novel Strategy for the Reduction of Coordinated Water in Prussian Blue Analogues for Their Application as Cathode Materials for Sodium-Ion Batteries," *Journal of Materials Chemistry A* 13, no. 16 (2025): 11848–11860.

18. A. Zhou, W. Cheng, W. Wang, et al., "Hexacyanoferrate-Type Prussian Blue Analogs: Principles and Advances Toward High-Performance Sodium and Potassium Ion Batteries," *Advanced Energy Materials* 11, no. 2 (2021): 2000943.

19. Q. Wang, W. Wang, Z. Xing, et al., "Sodium Salt Assisted Room-Temperature Synthesis of Prussian Blue Analogues as High-Performance Cathodes for Sodium-Ion Batteries," *Applied Surface Science* 669 (2024): 160499.

20. H. Zhang, Y. Gao, J. Peng, et al., "Prussian Blue Analogues with Optimized Crystal Plane Orientation and Low Crystal Defects toward 450 Wh Kg^{-1} Alkali-Ion Batteries," *Angewandte Chemie International Edition* 62, no. 27 (2023): e202303953.

21. X. Wu, W. Deng, J. Qian, Y. Cao, X. Ai, and H. Yang, "Single-crystal FeFe(CN)6 nanoparticles: a high capacity and high rate cathode for Na-ion batteries," *Journal of Materials Chemistry A* 1, no. 35 (2013): 10130–10134.

22. M. J. Piernas Muñoz and E. Castillo Martínez, Prussian Blue Based Batteries, (Springer International Publishing, 2018), http://link.springer.com/10.1007/978-3-319-91488-6.

23. J. Chen, K. Huang, and S. Liu, "Insoluble Metal Hexacyanoferrates as Supercapacitor Electrodes," *Electrochemistry Communications* 10, no. 12 (2008): 1851–1855.

24. D. Schäfer, K. Hankins, M. Allion, et al., "Multiscale Investigation of Sodium-Ion Battery Anodes: Analytical Techniques and Applications," *Advanced Energy Materials* 14, no. 15 (2024): 2302830.

25. Z. Choi, D. Kramer, and R. Mönig, "Correlation of Stress and Structural Evolution in Li4Ti5O12-Based Electrodes for Lithium Ion Batteries," *Journal of Power Sources* 240 (2013): 245–251.

26. G. G. Stoney, "The Tension of Metallic Films Deposited by Electrolysis," *Proceedings of the Royal Society of London. Series A, Containing Papers of a Mathematical and Physical Character* 82, no. 553 (1909): 172–175.

27. L. Sbrascini, A. Sarapulova, C. Gauckler, et al., "Effect of Presodiation Additive on Structural and Interfacial Stability of Hard Carbon | P2-Na0.66Mn0.75Ni0.2Mg0.05O2 Full Cell," *Batteries & Supercaps* 7, no. 12 (2024): e202400207.

28. X. Wu, M. Shao, C. Wu, et al., "Low Defect FeFe(CN)6 Framework as Stable Host Material for High Performance Li-Ion Batteries," *ACS Applied Materials & Interfaces* 8, no. 36 (2016): 23706–23712.

29. L. Shen, Z. Wang, and L. Chen, "Prussian Blues as a Cathode Material for Lithium Ion Batteries," *Chemistry – A European Journal* 20, no. 39 (2014): 12559–12562.

30. X. Liu, Y. Cao, and J. Sun, "Defect Engineering in Prussian Blue Analogs for High-Performance Sodium-Ion Batteries," *Advanced Energy Materials* 12, no. 46 (2022): 2202532.

31. W. Wang, Y. Gang, J. Peng, et al., "Effect of Eliminating Water in Prussian Blue Cathode for Sodium-Ion Batteries," *Advanced Functional Materials* 32, no. 25 (2022): 2111727.

32. Q. Liu, Z. Hu, M. Chen, et al., "The Cathode Choice for Commercialization of Sodium-Ion Batteries: Layered Transition Metal Oxides versus Prussian Blue Analogs," *Advanced Functional Materials* 30, no. 14 (2020): 1909530.

33. J. Sterzinger, R. Streng, S. Chen, et al., "Degradation Mechanisms of Prussian Blue Analogues and State-of-the-Art Approaches for Stability Optimization: A Review," *The Journal of Physical Chemistry C* 129, no. 15 (2025): 7135–7153.

34. Y. You, X. Yu, Y. Yin, K. W. Nam, and Y. G. Guo, "Sodium Iron Hexacyanoferrate with High Na Content as a Na-Rich Cathode Material for Na-Ion Batteries," *Nano Research* 8, no. 1 (2015): 117–128.

35. J. Cattermull, M. Pasta, and A. L. Goodwin, "Structural Complexity in Prussian Blue Analogues," *Materials Horizons* 8, no. 12 (2021): 3178–3186.

36. L. Ge, Y. Song, P. Niu, et al., "Elaborating the Crystal Water of Prussian Blue for Outstanding Performance of Sodium Ion Batteries," *ACS Nano* 18, no. 4 (2024): 3542–3552.

37. Y. Lu, L. Wang, J. Cheng, and J. B. Goodenough, "Prussian Blue: A New Framework of Electrode Materials for Sodium Batteries," *Chemical Communications* 48, no. 52 (2012): 6544–6546.

38. D. O. Ojwang, L. Häggström, T. Ericsson, R. Mogensen, and W. R. Brant, "Guest Water Hinders Sodium-Ion Diffusion in Low-Defect Berlin Green Cathode Material," *Dalton Transactions* 51, no. 38 (2022): 14712–14720.

39. M. Wan, R. Zeng, J. Meng, et al., "Post-Synthetic and In Situ Vacancy Repairing of Iron Hexacyanoferrate Toward Highly Stable Cathodes for Sodium-Ion Batteries," *Nano-Micro Letters* 14, no. 1 (2022): 9.

40. Y. Yang, E. Liu, X. Yan, et al., "Influence of Structural Imperfection on Electrochemical Behavior of Prussian Blue Cathode Materials for Sodium Ion Batteries," *Journal of the Electrochemical Society* 163, no. 9 (2016): A2117.

41. Y. You, X. L. Wu, Y. X. Yin, and Y. G. Guo, "High-Quality Prussian Blue Crystals as Superior Cathode Materials for Room-Temperature Sodium-Ion Batteries," *Energy & Environmental Science* 7, no. 5 (2014): 1643–1647.

42. J. Y. Heo, J. H. Lee, G. Kim, H. Kim, H. J. Lee, and J. H. Lee, "The Role of Carrier Ion-Ligand Interaction on Intercalation Potentials and Phase Evolution of Berlin Green Cathodes in Rechargeable Batteries," *Advanced Functional Materials* 34, no. 49 (2024): 2409171.

43. H. Li, J. Huang, K. Yang, et al., "Operando Electrochemical X-Ray Diffraction and Raman Spectroscopic Studies Revealing the Alkali-Metal Ion Intercalation Mechanism in Prussian Blue Analogues," *The Journal of Physical Chemistry Letters* 13, no. 2 (2022): 479–485.

44. C. Ling, J. Chen, and F. Mizuno, "First-Principles Study of Alkali and Alkaline Earth Ion Intercalation in Iron Hexacyanoferrate: The Important Role of Ionic Radius," *The Journal of Physical Chemistry C* 117, no. 41 (2013): 21158–21165.

45. A. Hofmann, F. Müller, S. Schöner, and F. Jeschull, "Revealing the Formation of Dialkyl Dioxahexane Dioate Products from Ethylene Carbonate Based Electrolytes on Lithium and Potassium Surfaces," *Batteries & Supercaps* 6, no. 12 (2023): e202300325.

46. I. Panasenko, M. Bäuerle, and F. Jeschull, "How Reference Electrodes Improve Our Understanding of Degradation Processes in Half and Full Cell Potassium-Ion Battery Setups," *Electrochimica Acta* 513 (2025): 145551.

47. T. Brendel, M. Janzen, M. Müller, W. Bauer, D. Kramer, and R. Mönig, "The Dynamics of the Structure of Composite Electrodes during Their Operation in Lithium-Ion Batteries," *Energy Technology* 13 (2025): 2500106.

48. W. H. Woodford, W. C. Carter, and Y. M. Chiang, "Strategies to Avert Electrochemical Shock and Their Demonstration in Spinels," *Journal of the Electrochemical Society* 161, no. 11 (2014): F3005.

49. Y. Xiao, J. Xiao, H. Zhao, et al., "Prussian Blue Analogues for Sodium-Ion Battery Cathodes: A Review of Mechanistic Insights, Current Challenges, and Future Pathways," *Small* 20, no. 35 (2024): 2401957.

50. S. Baumgart, M. Sotoudeh, I. E. Castelli, and A. Groß, "Improved Calculation Framework for Prussian Blue Analogues as a Battery Material," *EES Batteries* 2 (2026): 220–237, https://pubs.rsc.org/en/content/articlelanding/2026/eb/d5eb00211g.

51. Y. He, S. L. Dreyer, T. Akçay, et al., "Leveraging Entropy and Crystal Structure Engineering in Prussian Blue Analogue Cathodes for Advancing Sodium-Ion Batteries," *ACS Nano* 18, no. 35 (2024): 24441–24457.

52. Z. Zhang, M. Avdeev, H. Chen, W. Yin, W. H. Kan, and G. He, "Lithiated Prussian Blue Analogues as Positive Electrode Active Materials for Stable Non-Aqueous Lithium-Ion Batteries," *Nature Communications* 13, no. 1 (2022): 7790.

53. H. L. B.Boström and W. R.Brant, "Octahedral Tilting in Prussian Blue Analogues," *Journal of Materials Chemistry C* 10, no. 37 (2022): 13690–13699.

54. J. Y. Liao, Q. Hu, B. K. Zou, J. X. Xiang, and C. H. Chen, "The Role of Potassium Ions in Iron Hexacyanoferrate as a Cathode Material for Hybrid Ion Batteries," *Electrochimica Acta* 220 (2016): 114–121.

55. J. Cattermull, N. Roth, S. J. Cassidy, M. Pasta, and A. L. Goodwin, "K-Ion Slides in Prussian Blue Analogues," *Journal of the American Chemical Society* 145, no. 44 (2023): 24249–24259.

56. T. Hosaka, K. Kubota, A. S. Hameed, and S. Komaba, "Research Development on K-Ion Batteries," *Chemical Reviews* 120, no. 14 (2020): 6358–6466.

57. X. Bie, K. Kubota, T. Hosaka, K. Chihara, and S. Komaba, "A Novel K-Ion Battery: Hexacyanoferrate(ii)/Graphite Cell," *Journal of Materials Chemistry A* 5, no. 9 (2017): 4325–4330.

Supporting Information

Additional supporting information can be found online in the Supporting Information section.